Granular Matter (2009) 11:209–220
DOI 10.1007/s10035-009-0142-6

Flow–obstacle interaction in rapid granular avalanches: DEM simulation and comparison with experiment

Harald Teufelsbauer · Y. Wang · M. -C. Chiou · W. Wu

Received: 26 August 2008 / Published online: 6 May 2009

Abstract This paper investigates the interaction between rapid granular flow and an obstacle. The distinct element method (DEM) is used to simulate the flow regimes observed in laboratory experiments. The relationship between the particle properties and the overall flow behaviour is obtained by using the DEM with a simple linear contact model. The flow regime is primarily controlled by the particle friction, viscous normal damping and particle rotation rather than the contact stiffness. Rolling constriction is introduced to account for dispersive flow. The velocity depth-profiles around the obstacles are not uniform but varying over the depth. The numerical results are compared with laboratory experiments of chute flow with dry granular material. Some important model parameters are obtained, which can be used to optimize defense structures in alpine regions.

Keywords Granular material · Avalanche flow · Avalanche defense structures · Chute flow · Flow–obstacle interaction · Numerical simulation · Distinct element method

1 Introduction

Snow avalanche is the major form of natural hazards in alpine regions. The numerical modelling of snow avalanches is of current research interest [1,3,29,32,35,41]. Snow avalanches can be modelled by either continuum or discrete approaches. In continuum approaches, snow is often treated as a plastic material or a viscous fluid. The underlying problem can be simplified by adopting different assumptions, e.g. one-dimensional or two-dimensional depth-averaged models [21,26,35,36,40,42]. In discrete approaches, snow is modelled by an assemblage of discrete particles [2,17]. The motion of particles and the interaction among them obey the basic laws of motion. Other approaches in modelling snow avalanches include cellular automata [1], the lattice Boltzmann method [46] and the particle finite element method [33].

Avalanche protection often involves complex interaction between avalanche and retaining structures. Little work has been done on the flow/structure interaction due to the complexity of the underlying problem. A numerical study following the depth integrated approach [40] was reported by Chiou et al. [7]. Some promising results were obtained by using the high resolution TVD-NOC (total variation diminishing non-oscillatory central) integration scheme. For general obstacle geometries, however, the applicability of the depth integrated approach remains questionable. The flow of dense granular material around an immersed cylinder was experimentally investigated by Chehata et al. [6] focusing on the drag force on the cylinder. Chiou [8] reported a series of experiments on the deposition behaviour around obstacles and in the run-out zone. Recently, the drag force on an immersed cylinder in a dilute granular flow was studied with the DEM by Bharadwaj et al. [2]. While these investigations provide some interesting insights into the complex interaction between granular flow and obstacle, they also bring some fundamental questions to light. What is the effect of an obstacle in the different flow regimes, from the stagnation zone in front of the obstacle to the rapid flow in the far field? Can granular avalanches of angular particles be modelled by spherical particles in DEM? What is the three-dimensional structure of flow

---

H. Teufelsbauer (✉) · Y. Wang · W. Wu
Institute of Geotechnical Engineering,
University of Natural Resources and Applied Life Sciences,
Feistmantelstraße 4, 1180 Vienna, Austria
e-mail: harald.teufelsbauer@boku.ac.at

Y. Wang · M.-C. Chiou
Department of Mechanical Engineering,
Darmstadt University of Technology,
Hochschulstraße 1, 64289 Darmstadt, Germany

around an obstacle? What is the deposition behaviour beyond an obstacle and in the run-out zone? These questions have motivated us to carry out some numerical simulations with the DEM.

2 Problem description, chute geometry and parameters

We investigate granular flow driven by gravity down an incline and the interaction between flow and an obstacle in the chute. The parameters in a DEM calculation need to be identified by comparing the numerical results with some benchmark experiments. The model tests reported by Chiou [8] are well suited for our purpose. There are a number of advantages of well instrumented model tests in laboratory over field measurements of snow avalanches. In laboratory tests, the results can be well reproduced with well defined initial and boundary conditions. Another advantage of laboratory chute experiments is the possibility to change the topographical features like inclination angle, dam position and dimension of the dam. The effect of topography on granular flow and deposition can be investigated by varying the dam position and chute inclination. Similarly, the type and the amount of the granular material and initial flow configuration can easily be controlled in the laboratory avalanche experiments.

The cross section of the chute geometry for the model tests [8] is shown in Fig. 1. The same geometry is also used in the DEM calculations. The chute is divided into three parts: the upper inclined zone, the circular transition zone and the horizontal run-out zone. The inclination angle ζ of the upper inclined zone can be adjusted to 30°, 40°, 45° and 50°. If the inclination angle is zero the chute forms a flat plane with a total length of 1915 mm. The chute width is about 1.1 m.

Table 1 provides the dimensions of the chute for different inclination angles ζ. The granular material is held initially at the position l_4, by a hemispherical cap (see Fig. 1). Granular flow is initiated by lifting the cap suddenly [37]. This flow initiation is simulated in the DEM calculations.

An obstacle (cuboid dam) is mounted onto the chute surface in the inclined zone (see Fig. 1). Apparently, the impact velocity of granular flow on the obstacle depends on the position of the obstacle. For this reason, two dam positions are considered, i.e. $P_1 = 650$ mm and $P_2 = 810$ mm (see Fig. 1). In order to obtain a symmetrical flow pattern, the dam is placed in the center of the chute. Three dam heights are investigated. The dimensions are given in Table 2.

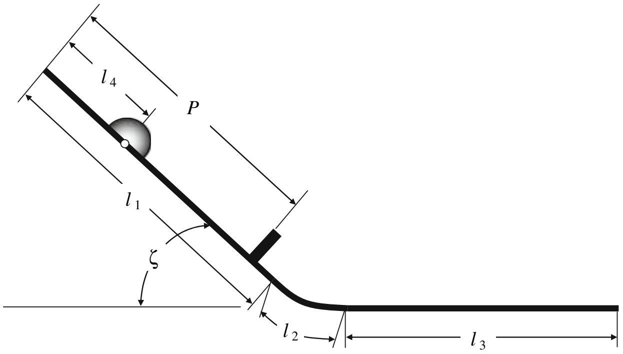

Fig. 1 Cross section along the center of the chute

Table 1 Geometry of chute and hemispherical cap (mm)

Chute detail	Inclination angle ζ	
	40°	45°
Upper inclined part, l_1	933.5	936
Transition zone, l_2	146.5	144
Horizontal run-out zone, l_3	835	835
Chute width	1100	1100
Cap position, l_4	309.5	312
Cap radius	100	100

Table 2 Geometry of cuboid dams (mm)

Dams	Dam dimension		
	Width	Height	Thickness
Lower dam	160	20	10
Intermediate dam	160	40	10
Higher dam	160	80	10

Granular materials are characterized by density, restitution coefficient and internal- and basal friction angles [8,40]. Chiou [8] used coarse quartz sand with a mean diameter of 5 mm, a material density of 2650 kg/m^3 and a restitution coefficient of about 0.75.

3 Discrete element model

The numerical calculations are carried out with the commercial software PFC3d (particle flow code in three dimensions [22]). PFC3d is a simulation tool based on the distinct element method [4] and can model the dynamic motion and interaction of assemblies of arbitrarily sized spherical particles. The distinct elements, so-called balls, interact with each other based on a force-displacement law and Newton's second law of motion. Besides balls, PFC3d provides also wall elements, which allow the creation of static boundary elements. The displacements of colliding particles are represented by the overlap of the particles, and the interaction forces between the particles depend on the overlap. The forces between particles during contact are calculated according to some simple mechanical models such as springs and dashpots [5,25,30]. Usually, the contact force is decomposed into a normal and a shear component. The material properties of the discrete elements (balls and walls) are characterized by the stiffness and friction. In addition, the balls are characterized by the ball radii and densities.

The normal and shear forces between particles and between particles and the wall are governed by the Kelvin–Voigt model. This model consists of an elastic spring and a viscous damper connected in parallel. The viscous damping controls the energy dissipation during particle collision. Taking the normal force as example, the viscous damping can be related to the coefficient of restitution as follows [4,22,43,44]:

$$\eta_n = -\frac{\ln(\varepsilon)}{\sqrt{\ln^2(\varepsilon) + \pi^2}}, \tag{1}$$

where η_n is the viscous damping and ε is the restitution coefficient. The coefficient of restitution can be measured in laboratory and defines the ratio between impact velocity and rebound velocity. Besides viscous damping, PFC3d offers also the local damping, which gives rise to a damping-force term to the equation of motion. For gravity-driven flows the local damping is set equal to zero which implies free fall without drag.

Both the normal and shear forces are subjected to some restrictions. For cohesionless granular materials the normal force is restricted to be compressive only, i.e. tensile normal force is not allowed. The allowable tangential force is assumed to obey the Coulomb friction law, which can be expressed by a linear relationship between the normal force F^n and the allowable shear force $F^s_{\max}$

$$F^s_{\max} = \mu \left| F^n \right|, \tag{2}$$

where μ is the friction coefficient. Slip between two adjacent particles occurs, if the shear force is equal to the allowable shear force. In a first approximation the friction coefficient μ between particles can be related to the internal friction angle ϕ through $\mu = \tan\phi$. The friction coefficient between particle and wall can be estimated analogously by replacing the wall friction angle δ with the internal friction angle ϕ. These are material parameters whose values are measured in the laboratory [37,38,40]. Alternatively, these parameters can also be obtained by back analyses [50].

4 Parameter identification

The parameters in PFC3d can be classified into ball properties, wall properties, damping properties and user defined parameters. The properties of balls are described by the density ρ, the friction angle ϕ, the normal- and shear stiffnesses k^B_n, k^B_s and the ball diameter d. The walls are characterized by the wall friction angle δ and the wall normal- and shear-stiffnesses k^W_n, k^W_s, respectively. The damping properties describe energy dissipation and can be compared with mechanical damping elements. PFC3d provides two kinds of damping, the local damping η_l and the viscous damping ratio in the normal and tangential direction η_n, η_s, respectively.

In principle, the ball density can be assumed to be equal to the density of quartz. However, a slightly different density is used in PFC3d, because the void ratio in DEM differs from the experiments. Since the total mass of the granular material in the release cap is of primary interest and not the density of the individual particles, the ball density is chosen to fit the total mass in the release cap. This gives rise to a particle density of about $\rho = 2900$ kg/m^3, which can be compared to the quartz bulk density of 2650 kg/m^3. The quartz particles used in the laboratory experiments are approximately monodispersed and have a mean diameter of 5 mm ± 1 mm [8,37,38]. Correspondingly, the diameters of the balls in PFC are uniformly distributed in the interval between 4 and 6 mm.

The local damping η_l is set to zero because the drag force on the particles caused by air is negligible. The critical damping ratio in normal direction η_n is related to the restitution coefficient of the granular material via (1). Some parametric studies have been carried out on the viscous shear damping η_s by comparing the run-out distance and travel time with experiments. These parameter studies showed that viscous shear damping has only minor influence on the flow in the inclined zone. If shear damping is set to zero, the avalanche becomes highly dispersed in the run-out zone. A higher shear damping results in delayed scattering of the avalanche. However, the shear damping has only little effect on the run-out distance.

We turn to explain the derivation of the particle stiffness which is used in the linear contact model and relates the contact force and relative displacement. Our parameter studies showed that the behavior of granular avalanches is not sensitive to the particle stiffness. It is known that high particle stiffness gives rise to long computation time [22]. The contact stiffness of two colliding particles can be calculated by the Hertzian theory. PFC provides two contact models, the linear model and the Hertz–Mindlin model [22,30]. For the latter the following equation provides the correlation between the normal contact stiffness k_n and the particle overlap u.

$$k_n = \frac{2G\sqrt{2\tilde{R}}}{3(1-v)} u^{1/2} \tag{3}$$

where G is the shear modulus, v is the Poisson's ratio and $\tilde{R}$ is the mean particle radius of two colliding particles. Since the Hertz–Mindlin contact model needs more computational effort than the linear contact model, the latter is used for our calculations. The stiffness of the linear contact model can be related to the Hertzian stress by the following consideration. When two balls are colliding, the contact area increases with increasing particle overlap. The stiffness of the linear model is independent of the particle overlap.

In order to estimate the stiffness for the linear contact model, a mean particle overlap has to be determined. The overlap can be obtained from the DEM calculations. At first, one calculation was carried out with the Hertz–Mindlin contact model in order to obtain the mean particle overlap. The properties of quartz are $\upsilon = 0.3$ and $G = 2.9 \cdot 10^{10}$ Pa [19]. The particle overlap was then estimated for three different flow regimes. The first overlap estimate was made at the beginning of the simulation when all particles were at rest (see Fig. 4a). The mean overlap of all particles in contact with each other was about $u_1 = 1 \cdot 10^{-8}$ m. The second overlap estimation of about $u_2 = 0.5 \cdot 10^{-8}$ m was made when the avalanche flow was fully developed and the particles were moving down the chute (see Fig. 4b). This second estimation represents the particle overlap at rapid flow. The third estimate ($u_3 = 1.5 \cdot 10^{-8}$ m) represents the particle overlap at the final deposition of the avalanche (Fig. 4c). It was observed that the particle overlap is nearly independent of the flow regime. The mean particle overlap u, used for further calculations is taken as the arithmetic mean of the three estimates: $u = (u_1 + u_2 + u_3)/3 = 10^{-8}$ m.

Based on the particle overlap obtained by the Hertz–Mindlin model, the radius of the resulting contact area r_c can be calculated as the cross section of a cylindrical rod with length d, which represents the distance between the centers of the two colliding particles (Fig. 2). Hence, the contact normal stiffness k_n of the linear model can be readily derived

$$k_n = \frac{r_c^2 \pi \ E}{d}, \tag{4}$$

where $E = 2G(1 + \upsilon)$ is Young's modulus. The radius r_c of the contact area can be related to the particle overlap as follows

$$r_c = \sqrt{2h\frac{d}{2} - h^2}, \quad \text{with } h = \frac{u}{2}. \tag{5}$$

The Young modulus of quartz is about $E = 7.6 \cdot 10^{10}$ Pa. It follows that the contact stiffness of $k_n = 1200$ N/m can be assumed for the linear model. The relation between the ball stiffness and contact stiffness is given by [19]:

$$k_j = \frac{k_j^{[B1]} \cdot k_j^{[B2]}}{k_j^{[B1]} + k_j^{[B2]}}, \tag{6}$$

where k_j is the contact stiffness and $k_j^{[B1]}$, $k_j^{[B2]}$ are the stiffnesses of ball 1 and ball 2, respectively. The subscripts $j = n$ and $j = s$ stand for normal and shear direction, respectively. As an example, if the two colliding balls have the same stiffness, $k_j^B = k_j^{[B1]} = k_j^{[B2]}$, the ball stiffness is twice the contact stiffness $k_j^B = 2k_j$.

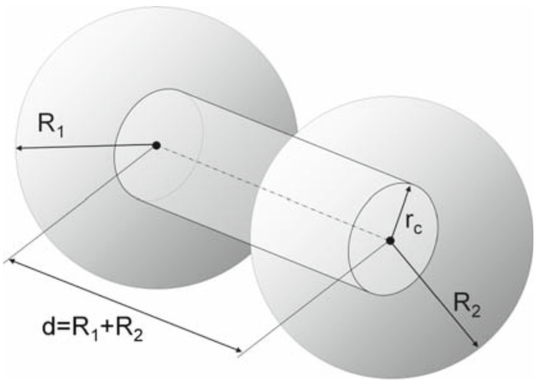

Fig. 2 Hertzian contact stress idealized as a rod connecting ball centers

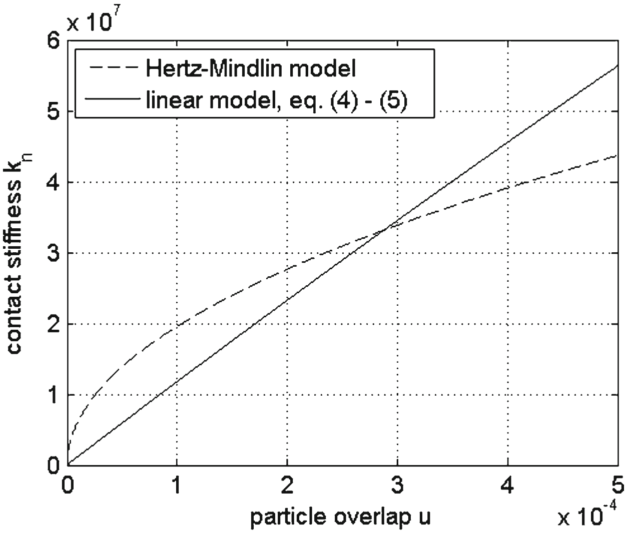

Fig. 3 Comparison between linear contact model and Hertz–Mindlin contact model

A comparison between the contact stiffness calculated by the Hertz–Mindlin contact model and the stiffness of a cylindrical rod ((4), (5)) is shown in Fig. 3. It can be seen that for small particle overlaps the stiffness of the cylindrical rod is smaller than the stiffness of the Hertz–Mindlin model. Several calculations with different contact stiffness ranging from 500 to 10,000 N/m were performed in order to investigate the sensitivity of the flow regime on the normal stiffness. These case studies showed that the contact stiffness has only minor influence on the behavior of granular avalanches. This remains so for a variation of the normal stiffness by a factor of 20. Furthermore, for overlaps $h < 10^{-4}$ m the relation between particle overlap and rod stiffness is nearly linear. It follows that the deviation of the three estimated particle overlaps u_1, u_2, u_3 for the three different flow regimes has only minor effects on the flow behavior.

The shear stiffness k_s is assumed to be equal to the normal stiffness k_n. Admittedly, this assumption is a crude approximation. However, numerical calculations showed that the flow regime is fairly independent on the contact shear stiffness.

Comparison between numerical results and laboratory experiments shows that the flow propagation is mainly dictated by the magnitude of viscous normal damping η_n and particle rotation. These two parameters are crucial for describing the dispersive behavior of the granular flow. If particles are free in rotation, friction coefficients and contact shear stiffness are of minor importance. However, if the rotation is constrained and only sliding is allowed, the system is very sensitive to friction coefficient. Free or nearly free rotations can be observed in particles with few contacts or even no contact with other particles. In this case the particle rotation is not restrained by the surrounding particles. Note that particle spin becomes effective only in dispersive flow rather than in dense flow, except in the vicinity of the dam and in agitated margin. The particles in dense flow show virtually no spin. The granular mass slides down the incline as if it were a continuously deforming body [37,38,40].

In reality the quartz particles are not spherical while our calculations assume spherical particles. Rolling down an incline, a spherical particle will need much longer distance than a angular particle before it comes to standstill. As a consequence, the borders of the avalanche are more dispersive in the DEM simulations than in experiments [37–39]. Moreover, the shape of the deposition piles and the run out distance of the avalanche is strongly dependent on the rolling friction. Apparently, the particle rotation is crucial for modeling granular flows by DEM.

5 Observation of flow regimes

The flow regimes are investigated by some DEM simulations, which were carried out for different angles of chute inclination with and without particle constraint. These numerical simulations showed that the flow regime can be divided into two parts: the supercritical or torrential flow in the steep inclined zone and the subcritical or fluvial flow in the run-out zone. Furthermore, a different dispersive behavior of the flow could be observed, dependent on the type of granular material. The more dispersive a flow the fewer particles are contained per volume and the fewer contacts has a particle to its neighbors. In case of free rotation the borders of the avalanche are very dispersive especially in the run-out zone. This phenomenon can be explained by the fact that the wall friction is not high enough to stop the particles in the run out zone. Obviously the particle motion is dominated by rolling not by sliding. Therefore the ball and wall friction has minor effect on the run-out distance. As the quartz particles are not spherical, the particle motion should be described by a combination of sliding and rolling.

A sensitivity analysis of rolling friction, ball friction and wall friction was carried out. The following observations can be made: The influence of friction on the flow behavior seems to decrease with increasing chute inclination (also see, [40]). Since the driving force is dominated by gravitational acceleration, the influence of friction on steep inclined planes is not as important as for chutes with small inclinations. It follows that the flow behavior in the run-out zone is strongly dependent on friction, which can be further differentiated between rolling friction and Mohr–Coulomb friction (Sect. 3). Numerous parameter studies showed that the rolling friction has more influence on the flow behavior than Mohr–Coulomb friction. In the experiments with quartz particles, the rolling friction is very high. A detailed description of the rotation constraint is given in Sect. 6.

Further observations are concerned with the viscous damping [45,47], especially in the range between $0 < \eta_n < 0.1$. The influence of viscous damping is particularly noticeable when the avalanche hits an obstacle, since viscosity describes the rebound behavior of the particles. Higher viscosity gives rise to less dispersive behavior. Further simulations were carried out to study the combined effect of rotation constraint and viscosity. It turned out that viscous damping is appropriate to describe the impact behavior of particles on a wall or onto a heap of deposited particles, whereas the constraint of the particle rotation is appropriate to characterize the dispersive behavior of the dense flow along the chute. Laboratory experiments showed that the dispersive behavior of the flow depends on the properties of granular material and sliding surface. Furthermore, it was observed that dense flows have a less dispersed deposit than dilute flows. Hence, the particle rotation in DEM simulations should depend on material properties and whether the flow is dense or dilute. Figure 4 depicts the different processes of the avalanche flow along a chute.

As can be seen from Fig. 4a the granulates start to flow after the release cap is lifted. At this moment, the particles have many contacts with their neighbors. The flow is mainly governed by sliding.

When the granular flow along the inclined plane is fully developed (Fig. 4b) the granular mass can be divided in two parts: the densely packed mass in the center and the diluted regions around it. The particles within the central mass have many contacts to the surrounding particles and are therefore more constrained in rotation. On the contrary, the dilute particles around the central mass have only few contacts to their neighbors and are less constrained in rotation.

Upon hitting a dam, part of the granulates is held back in front of the dam (Fig. 4c). If the dam is sufficiently high, the particles cannot override the dam. In this case, the granular flow is split by the dam into two branches. When the particles reach the final deposition area, some of them may be able to override the deposition heap, while others stop at the deposition heap (Fig. 4c), see also [37–39].

Fig. 4 **a** Opening release cap—start of granular flow, **b** fully developed flow along the inclined zone, **c** impact on the dam and final deposition

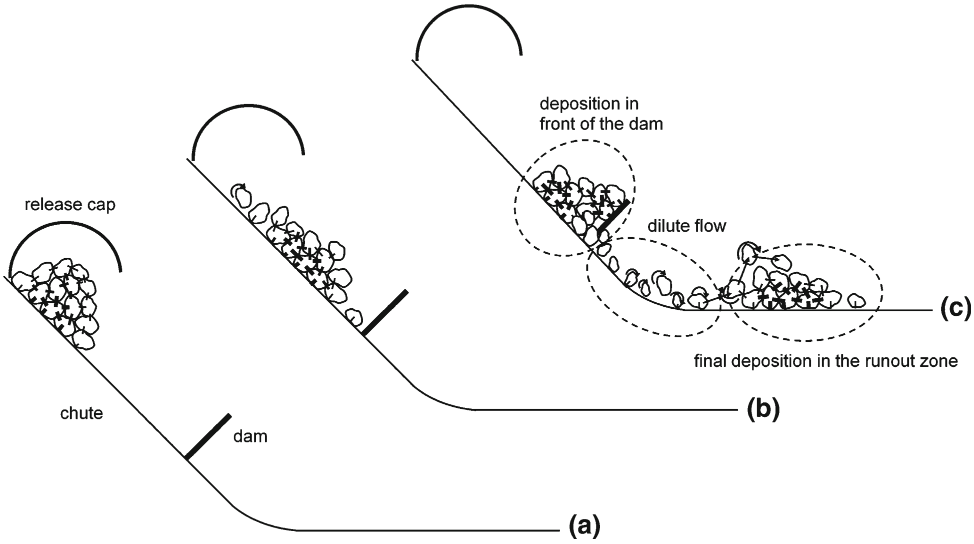

6 Rolling friction

As stated above, the rolling friction plays an important role in the DEM simulations. Comparison with experiments showed that the DEM simulations without rotation constraint yield too dispersive flow and deposition pattern particularly in the run-out zone. Obviously, the spherical particles in PFC3d need much longer distance to come to a standstill in the run-out zone. Improvement of the numerical calculations could be achieved by realistically modeling the angular quartz particles, which is, however, not feasible with PFC3d [34]. Since the rolling resistance of spherical particles is much smaller than that of angular particles, an artificial rolling resistance should be introduced into PFC3d [24,27,48,49].

The mechanism of rotation control in this paper is based on an empirical relationship between particle contacts and the constraint of particle rotation. The constraint of the particle rotation is described by a retarding coefficient k_λ and a retarding time λ. The retarding time λ defines the time span which is needed to reduce the angular velocity ω. The particle rotation in this time span is reduced by the retarding coefficient $k_\lambda \in [0,\ 1]$. The retarding coefficient is further related to the number of particle contacts. If a particle has neither contact to other particles nor to the chute surface, it is totally free in rotation and the retarding coefficient k_λ is equal to 1, i.e. the rotation is not constrained. If a particle has several contacts with other particles, the particle rotation will be constrained. The degree of constraint, i.e. k_λ, is proportional to the number of contacts. There are numerous experimental studies in soil mechanics on the contact number of spherical particles, see Feda [9]. For regular packings of monodispersive balls, the minimum number of contacts for the loosest packing is 6 and the maximum number of contacts for the densest packing is 12. For polydispersive particles, the number of contacts may vary in a broader range from 2 to 15. These findings were made on granular materials in static equilibrium. For flowing granular materials, there is hardly any experimental evidence on the contact number. Nonetheless, some plausible assumptions can be made. A simple assumption, although somewhat ad hoc, is to relate the particle rotation to the contact number c. To this end, the following relationship between the number of particle contacts c and the retarding coefficient k_λ is used

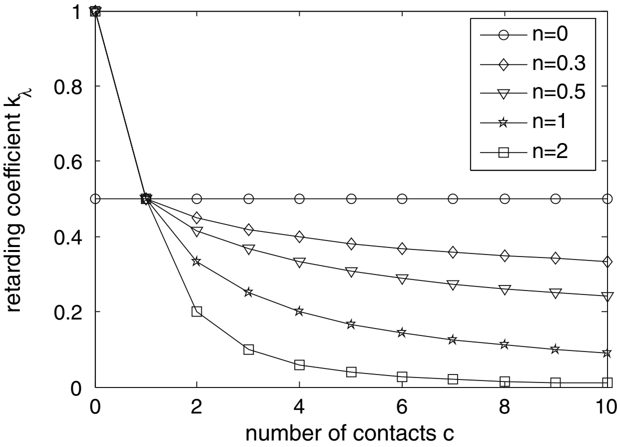

Fig. 5 Relation between contact number and retarding coefficient for different exponents n

$$k_\lambda = \frac{1}{1 + c^n}. \tag{7}$$

The parameter $n \geq 0$ governs the sensitivity of the retarding coefficient to the number of contacts. If $n = 0$ the retarding coefficient is independent of the number of contacts and $k_\lambda \equiv 0.5$. Larger n gives rise to stronger influence of the contact number (Fig. 5). If $n > 0$ and the number of contacts $c \geq 1$ the retarding coefficient k_λ is less than 0.5.

Note that the retarding coefficient provides no information about the time span, in which the rotation is reduced.

Fig. 6 Influence of exponent n to the flow regime (*left* $n = 0$, *right* $n = 4$). Snapshot taken at $t = 0.9$ s

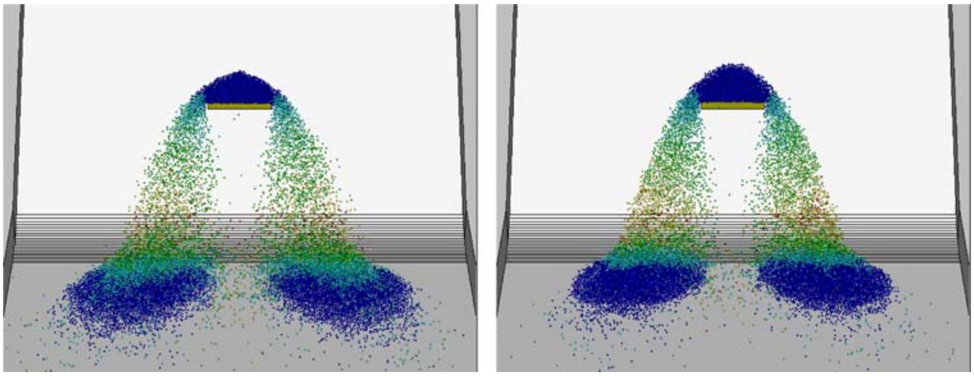

Fig. 7 Influence of retarding time λ to the flow regime (*left* $\lambda = 0.05$ s, *right* $\lambda = 0.001$ s). Snapshot taken at $t = 3.0$ s

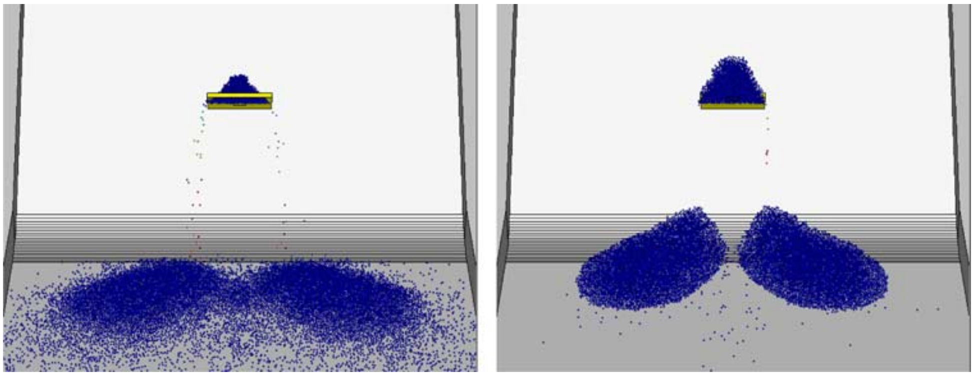

This is determined by the retarding time λ. If $\lambda \to 0$, the particle rotation is strongly constrained for $k_\lambda < 1$. Longer retarding time leads to less rotation constraint. In PFC3d, the rotations are obtained by integrating the equation of motion. The numerical integrations are performed in time steps. The length of the time step Δt is determined by particle stiffness and the relative velocities of the particles. An automatic control of the time steps is used in PFC3d. In order to calculate particle displacement and rotation, the equation of motion is solved in each time step using the calculated forces of the last step. In each time step the number of contacts of each particle is evaluated and the retarding coefficient k_λ is determined. Afterwards, the particle rotation ω_i^t in each direction $i = x, y, z$ is reduced to give the new rotation ω_i^{t+1}

$$\omega_i^{t+1} = k_\lambda^\xi \cdot \omega_i^t, \quad \text{with } \xi = \Delta t/\lambda, \tag{8}$$

where ξ denotes a time discretized retarding time λ. The discrete time steps in the chute experiments are in the order of $3 \cdot 10^{-5}$ s. It was found that a retarding time of $\lambda = 10^{-2}$ s and an exponent of n in a range $n \in [0.5, \ 1]$ lead to good agreement between simulations and experiment.

It is worth noting that other authors proposed to implement the rolling friction based on a torque model [24,27,48,49]

$$M = -\mu_r \, |F_n| \, \frac{\omega_i}{|\omega_i|}, \tag{9}$$

where μ_r is the coefficient of rolling friction and ω_i the angular velocity of the particle in the direction $i = 1, 2, 3$. Since the normal force F_n is dependent on the particle stiffness and viscous damping, the torque M is affected by the chosen particle stiffness. In order to avoid this dependency it is proposed to use the friction model in (8).

In Fig. 6, a comparison of the flow and deposition pattern for different exponents $n = 0$ and $n = 4$, introduced in (7) is shown. The granular stream is separated by the dam into two branches. These two branches are deposited in the run-out zone beyond the dam. Some particles are deposited in front of the dam. The particles in front of the dam and in the center of the deposition zones below the dam are densely packed. This is caused by the impacts of the subsequent particles. The granular stream between the dam and the deposition areas is rather dilute and particles here have only few contacts. A comparison between the depositions in the run-out zone (Fig. 6) shows that the borders of the deposition areas in the left panel ($n = 0$) are more dispersive than in the right panel ($n = 4$). Furthermore, the avalanche stops earlier for $n = 4$ because the rolling friction is higher for $n = 4$ than for $n, = 0$. Figure 6 shows further that the dilute flow between the dam and the deposition areas remains fairly of the exponent n.

Figure 7 shows the influence of the retarding time λ on the flow regime. For high retarding time with $\lambda = 0.05$ s the particles are nearly free in rotation, which results in highly dispersive flow (see the fuzzy borders in the left panel in

Fig. 7). For low retarding time with $\lambda = 0.001$ s the particles are highly constrained in rotation, which results in clear border and short run-out distances.

7 Comparison between DEM simulation and experiment

Figure 8 shows some snapshots of DEM simulation and experiment at different times after the granular heap is released. The snapshots are taken at the same times both in the DEM calculation and experiment. Visual inspection of the flow field shows good agreement between simulation and experiment. About 17.5% of the released granular mass was held back by the dam in the experiment. The numerical simulation came very close to the experiment with an accuracy of ±1.5%. The main features of granular flow in the inclined zone and deposition are well captured by the DEM.

Figure 8c shows that more particles flow towards the centre beyond the obstacle in experiment. We suppose that this is due to the jamming of the particles at the dam edge. The jamming is more pronounced for angular particles than for spherical particles. This is also confirmed by Fig. 8e. There is less granular material around the centre line in calculation than in experiment.

Further calculations were performed on a chute with an inclination of 45°. These calculations are aimed at studying the influence of the dam height on granular flow. The deposition of granular flow for three different dam heights is shown in Fig. 9. Comparison between experiment and simulation shows that the arrest of the material by the dam, the material overflow and the deposition geometry are well reproduced by the DEM simulation.

Comparison of the velocity field from simulation and experiment is shown in Fig. 10. The measurement of the surface velocity in the experiment was performed by PIV (particle image velocimetry) [37,38]. Some granulates are held back by the dam forming a dead zone in front of the dam [11–13,15]. The number of granulates in the dead zone increases with time until a stationary state is reached (Fig. 10a). As shown in Fig. 10b, the granular stream is separated by the dam into two branches. Comparison between PIV measurements and DEM simulation shows fairly good agreement of the velocity field. A detailed simulation of the dead zone in front of the dam is very important because the design of the protection structure depends on the dynamic impact on the dam and the granular mass in front of the dam. An important question in avalanche protection is the area of the protected zone below the retaining structure. The DEM model allows a reliable simulation of the protected zone below the dam.

The dynamics of avalanches is usually characterized by the so-called Froude number, which is the ratio between the characteristic velocity and the wave velocity. For shallow granular flow with free surface the Froude number can be expressed as follows:

$$Fr = \frac{v}{\sqrt{g \cos \varsigma h}}, \tag{10}$$

where v is the flow velocity of the avalanche surface, g the gravitational acceleration and h is the depth of avalanche. Figure 11 presents the spatial variation of the Froude number along the free surface of the granular flow. Effective protection against avalanches can be expressed in terms of the Froude number [13–16,18,20]. In the vicinity of the dam and also in the deposition zones, the avalanche transits from supercritical to subcritical flow. Moreover, the Froude number also serves as an indicator for the different flow regimes, i.e., to identify, where inertial or gravitational flow dominates. Furthermore, the Froude number allows the comparison of small scaled experiments to large-scale flow. Some field studies of natural avalanches shows that the Froude number is about 10 for dry and dense snow avalanches [28].

The influence of dam height on the flow pattern is shown in Fig. 11. In the following plots subcritical flow regime ($Fr < 1$) is plotted in white, whereas Froude numbers larger than one are depicted in a color spectrum. Figure 11a shows the flow pattern with an effective dam, where no overflow occurs. The Froude number in front of the dam is reduced to subcritical flow ($Fr < 1$), which is shown by the granulate deposition in front of the dam. Figure 11b shows the flow pattern with a low dam. In this case, the dam cannot dissipate enough energy and the Froude number remains high. It follows that the critical dam height with no overflow is associated with the development of a subcritical zone in front of the dam, which is clearly shown by the Froude numbers in front of the dam.

Figure 12 shows the side view of the granular flow in Fig. 11. As can be seen from Fig. 11a, a dead zone is formed in front of the 80 mm dam. Figure 11b shows the granular flow over the 20 mm dam. The dead zone is very small and forms a jump [20,23]. Moreover, the velocity of the overflowing part of the avalanche seems not to have been noticeably reduced. A perusal of Fig. 12 reveals that the velocity profile is fairly uniform normal to the chute, provided the flow field is not severely interrupted by the obstacle. However, the evaluation of the velocity profile around the dam indicates that the velocities are not uniformly distributed through the flow depth. This is one reason why continuum models based on depth integrated equations have their limits for problems involving interaction between granular flow and obstacles [10,38]. The distinct element method presents an alternative to such problems.

A simulation with rotation constraint takes about 10 h on a 3 GHz processor. For unconstrained flow the calculation was about three times faster. The number of particles was about 40,000. The computation of the rotation control leads

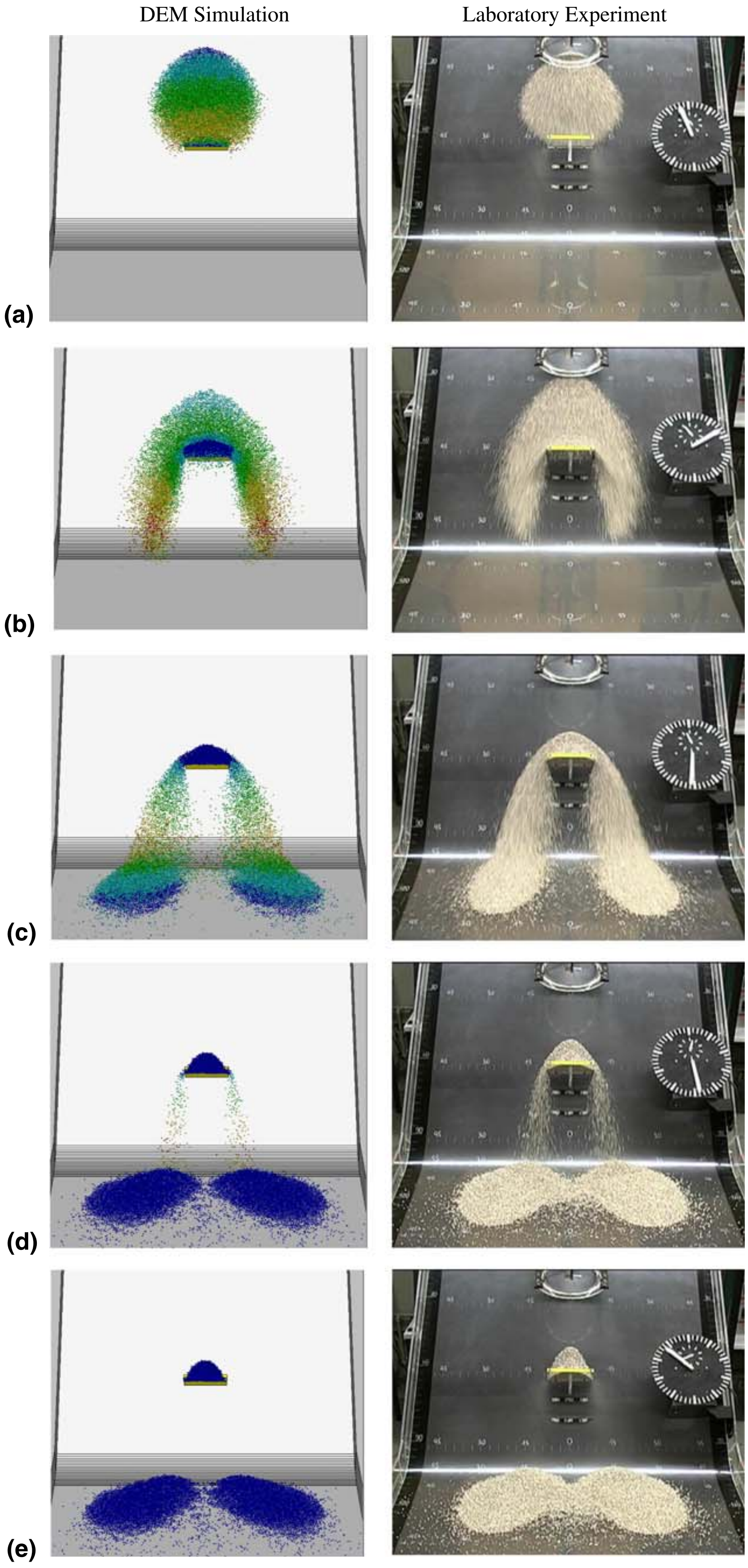

Fig. 8 Flow–obstacle interaction: comparison between the DEM simulation (*left panels*) and the laboratory experiment (*right panels*) with chute inclination of 40° and a dam at position P_1. The photographs of the laboratory experiments are taken from [8]. **a** $t = 0.28$ s, **b** $t = 0.56$ s, **c** $t = 0.84$ s, **d** $t = 1.8$ s, **e** $t = 8.2$ s

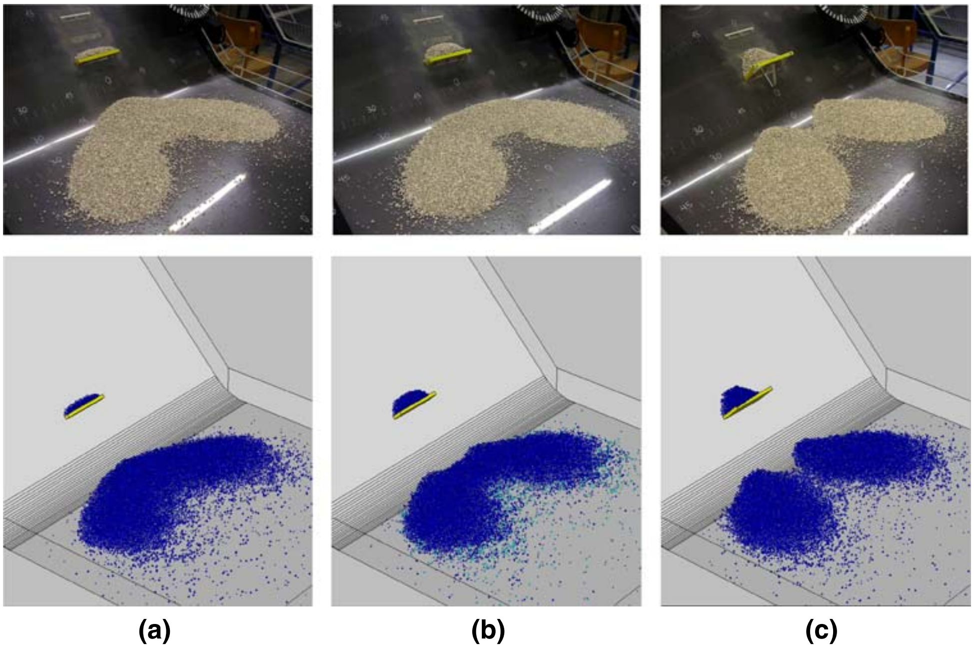

Fig. 9 Flow deposition: comparison between experiments (*top panels* [8]) and DEM calculations (*bottom panels*) in a 45° inclined chute with a dam at position P_2 with the dam height of **a** low dam, 20 mm, **b** intermediate dam, 40 mm and **c** high dam, 80 mm

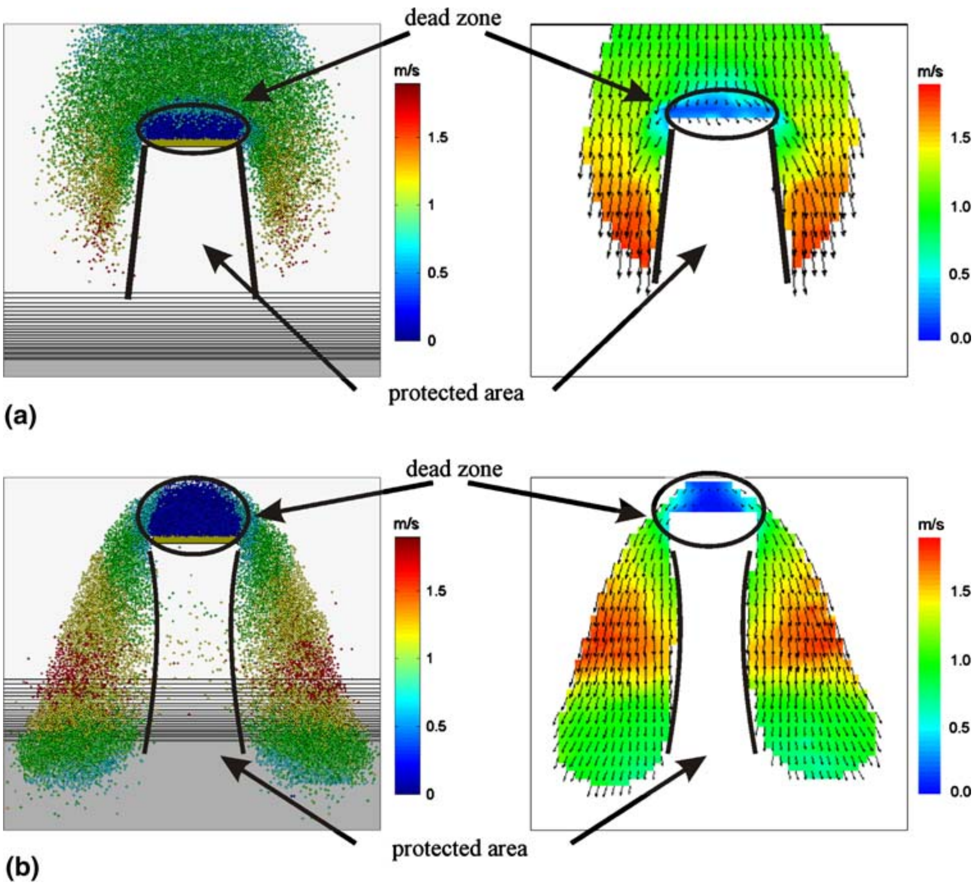

Fig. 10 Velocity profile: particle velocities (m/s) in the DEM calculation (*left panels*) and in the experiment (*right panels* [8]) at different time after cap lifting. The inclination of the chute is 40°, the dam is positioned at P_1 and the dam height is 80 mm. **a** $t = 0.38$ s, **b** $t = 0.66$ s

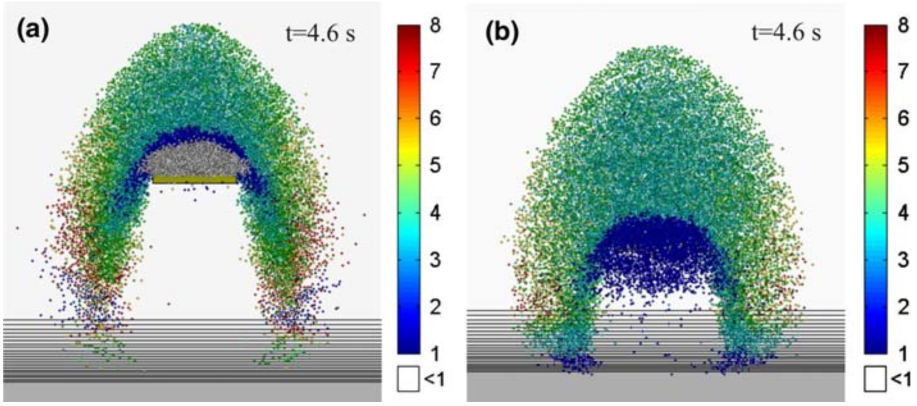

Fig. 11 The Froude number: **a** flow pattern on a 40° inclined chute with dam height of 80 mm at position P_1, **b** flow pattern on a 45° inclined chute with dam height of 20 mm at position P_2

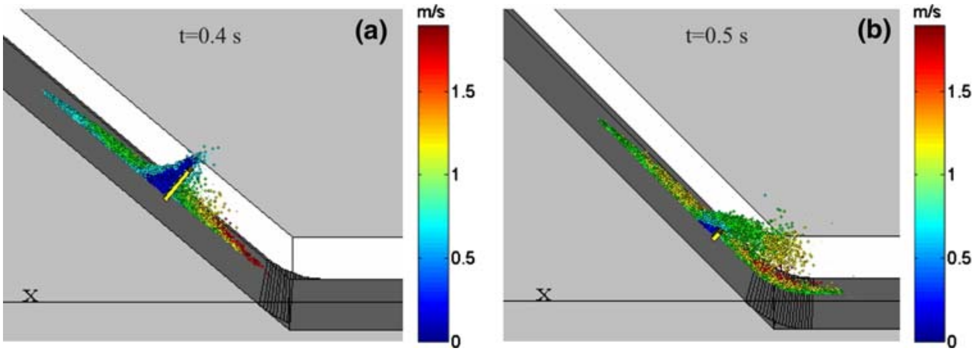

Fig. 12 Side view of the flow pattern in Fig. 11. **a** Flow pattern for a 80 mm dam at position P_1 on a 40° inclined chute, **b** flow pattern for a 20 mm dam at position P_2 on a 45° inclined chute

to increased CPU time because additional operations have to be performed in each time step.

8 Conclusion

The distinct element method can be applied to simulate granular flow and the interaction between granular flow and an obstacle. The simulations were compared with laboratory experiments. The comparison shows good agreement between simulation and experiment. The physical parameters, such as the internal and basal friction angles, density, particle diameter and restitution coefficient of the granulates were determined from laboratory experiments. The dispersive property of the granulate was determined by fitting the numerical simulation to experiment.

Some influence factors such as terrain form, dam geometry and dam position can be easily taken into consideration. Moreover, the DEM model can be applied to some situations where continuum approach fails, e.g. overflow of dam.

The viscous damping plays an important role in simulating flow-obstacle interactions. Both viscous damping and particle rotation have dominant effect on the dispersive behavior of granular flow. While the viscous damping is crucial in describing the particle impacts on the wall and on the deposited heap, the particle rotation plays a substantial role in the dispersive behavior of granular flow. Note that the impact force on dam is not treated here, which is needed in designing retaining structures. Some numerical results based on continuum approach [31] can be found in literature. Some calculations with DEM are being carried out to obtain the impact force on dam. The results will be presented in our next publication.

Acknowledgments The authors wish to thank FWF (Austrian Science Foundation) for the financial support through the project L351 “Numerical modeling towards innovative avalanche prevention” and S. P. Pudasaini for his assistance and helpful collaboration.

References

1. Barpi, F., Borri-Brunetto, M., Delli Veneri, L.: Cellular-automata model for dense-snow avalanches. J. Cold Reg. Eng. **21**, 121–140 (2007)
2. Bharadwaj, R., Wassgren, C., Zenit, R.: The unsteady drag force on a cylinder immersed in a dilute granular flow. Phys. Fluids **16**, 1511–1517 (2006)
3. Cantero, M.I., García, M.H., Balachandar, S.: Effect of particle inertia on the dynamics of depositional particulate density currents. Comput. Geosci. (2008, accepted)
4. Cundall, P.A., Strack, O.D.L.: A distinct element model for granular assemblies. Geotechnique **29**, 47–65 (1979)
5. Cundall, P.A.: Formulation of a three-dimensional Distinct Element Model. Part I. A scheme to detect and represent contacts in a system composed of many polyhedral blocks. Int. J. Rock Mech. Min. Sci. Geomech. Abstr. **25**(3), 107–116 (1988)

6. Chehata, D., Zenit, R., Wassgren, C.R.: Dense granular flow around an immersed cylinder. Phys. Fluids **15**, 1622–1631 (2003)
7. Chiou, M.C., Wang, Y., Hutter, K.: Influence of obstacles on rapid granular flows. Acta Mech. **175**, 105–122 (2005)
8. Chiou, M.C.: Modelling dry granular avalanches past different obstructs: numerical simulations and laboratory analyses, Dissertation. Technical University Darmstadt, Germany (2005)
9. Feda, J.: Mechanics of particulate materials. Elsevier, Amsterdam. ISBN: 978-0444997135 (1982)
10. Gray, J.M.N.T., Wieland, M., Hutter, K.: Gravity-driven free surface flow of granular avalanches over complex basal topography. Proc. R. Soc. A Math. Phys. Eng. Sci. **455**, 1841–1874 (1998)
11. Gray, J.M.N.T., Tai, Y.-C., Noelle, S.: Shock waves, dead-zones and particle-free regions in rapid granular free surface flows. J. Fluid Mech. **491**, 161–181 (2003)
12. Gray, J.M.N.T., Cui, X.: Weak, strong and detached oblique shocks in gravity-driven granular free-surface flows. J. Fluid Mech. **579**, 113–136 (2007)
13. Hákonardóttir, K.M., Hogg, A.J., Jóhannesson, T., Tómasson, G.G.: A laboratory study of the retarding effects of braking mounds on snow avalanches. J. Glaciol. **49**(165), 191–200 (2003)
14. Hákonardóttir, K.M., Hogg, A.J., Jóhannesson, T., Kern, M., Tiefenbacher, F.: Large-scale avalanche breaking mound and catching dam experiments with snow: a study of the airborne jet. Surv. Geophys. **24**, 543–554 (2003)
15. Hákonardóttir, K.M.: The interaction between snow avalanches and dams. PhD thesis, University of Bristol, School of Mathematics (2004)
16. Hákonardóttir, K.M., Hogg, A.J.: Oblique shocks in rapid granular flows. Phys. Fluids **17**, 077101 (2005). doi:10.1063/1.1950688
17. Hanes, D.M., Walton, O.R.: Simulations and physical measurements of glass spheres flowing down a bumpy incline. Powder Technol. **109**, 133–144 (2000)
18. Harbitz, C.B., Domaas, U., Engen, A.: Design of snow avalanche deflecting dams. Oslo, NGI, Report 589000-4. Also in: Proceedings of the 9th Interpraevent 2000 Congress, 26th–30th June 2000, Villach, Austria, vol. 1, pp. 383–396, 41 (2000)
19. Heaney, P.J., Prewitt, C.T., Gibbs, G.V.: Silica: physical behavior, geochemistry and materials applications. Rev. Mineral., vol. 29
20. Hungr, O., McClung, D.M.: An equation for calculating snow avalanche runup against barriers. Avalanche formation, movement and effects. In: Proceedings of the Davos Symposium, September 1986, vol. 162, pp. 605–612. IAHS Publ. (1987)
21. Hutter, K., Wang, Y., Pudasaini, S.P.: The Savage–Hutter avalanche model: how far can it be pushed? Phil. Trans. R. Soc. A Math. Phys. Eng. Sci. **363**, 1507–1528 (2005)
22. Itasca Consulting Group, Inc: PFC3D (Particle Flow Code in 3D) Theory and Background Manual, Version 3.0. ICG, Minneapolis (2003)
23. Jóhannesson, T.: Run-up of two avalanches on the deflecting dams at Flateyri, northwestern Iceland. Ann. Glaciol. **32**, 350–354 (2001)
24. Khan, K.M., Bushell, G.: Comment on rolling friction in the dynamic simulation of sandpile formation. Phys. A **352**, 522–524 (2005)
25. Kruggel-Emden, H., Simsek, E., Rickelt, S., Wirtz, S., Scherer, V.: Review and extension of normal force models for the Discrete Element Method. Powder Technol. **171**, 157–173 (2007)
26. Lehning, M., Doorschot, J., Bartelt, P.: A snowdrift index based on SNOWPACK model calculations. Ann. Glaciol. **31**, 382–386 (2000)
27. Li, S., Yao, Q., Chen, B., Zhang, X., Ding, Y.L.: Molecular dynamics simulation and continuum modelling of granular surface flow in rotating drums. Chin. Sci. Bull. **52**(5), 692–700 (2007)
28. McClung, D., Schaerer, P.: The Avalanche Handbook. The Mountaineers, Seattle (1993)
29. McElwaine, J., Nishimura, K.: Ping-pong ball avalanche experiments. Ann. Glaciol. **32**, 241–250 (2001)
30. Mindlin, R.D., Deresiewicz, H.: Elastic spheres in contact under varying oblique forces. J. Appl. Mech. **20**, 327–344 (1953)
31. Moriguchi, S., Borja, R.I., Yashima, A., Sawada, K.: Estimating the impact force generated by granular flow on a rigid obstruction. Acta Geotech. **4**, 57–71 (2009)
32. Nicot, F.: Constitutive modelling of snow as a cohesive-granular material. Granul. Matter **6**, 47–60 (2004)
33. Oñate, E., Celigueta, M.A., Idelsohn, S.R.: Modeling bed erosion in free surface flows by the particle finite element method. Acta Geotech. **1**, 237–252 (2007)
34. Peña, A.A., García-Rojo, R., Herrmann, H.J.: Influence of particle shape on sheared dense granular media. Granul. Matter **9**, 279–291 (2007)
35. Pitman, E.B., de Long, L.E.: A two-fluid model for avalanche and debris flows. Phil. Trans. R. Soc. A Math. Phys. Eng. Sci. **363**, 1573–1601 (2005)
36. Pudasaini, S.P., Hutter, K.: Rapid Shear flows of dry granular masses down curved and twisted channels. J. Fluid Mech. **495**, 193–208 (2003)
37. Pudasaini, S.P., Hsiau, S., Wang, Y., Hutter, K.: Velocity measurements in dry granular avalanches using Particle Image Velocimetry-Technique and comparison with theoretical predictions. Phys. Fluids **17**(9) (2005)
38. Pudasaini, S.P., Hutter, K., Hsiau, S., Tai, S., Wang, Y., Katzenbach, R.: Rapid flow of dry granular materials down inclined chutes impinging on rigid walls. Phys. Fluids **19**(5) (2007)
39. Pudasaini, S.P., Wang, Y., Sheng, L., Hsiau, S., Hutter, K., Katzenbach, R.: Avalanching granular flows down curved and twisted channels: theoretical and experimental results. Phys. Fluids **20**(7) (2008)
40. Pudasaini, S.P., Hutter, K.: Avalanche Dynamics: Dynamics of Rapid Flows of Dense Granular Avalanches. Springer, Berlin (2007)
41. Sailer, R., Fellin, W., Fromm, R., Jor̈g, P., Rammer, L., Sampl, P., Schaffhauser, A.: Snow avalanche mass-balance calculation and simulation-model verification. Ann. Glaciol. **48**, 183–192 (2008)
42. Savage, S.B., Hutter, K.: The motion of a finite mass of granular material down a rough incline. J. Fluid Mech. **199**, 177–215 (1989)
43. Schwager, T., Pöschel, T.: Coefficient of restitution and linear–dashpot model revisited. Granul. Matter **9**, 465–469 (2007)
44. Schwager, T., Pöschel, T.: Coefficient of restitution for viscoelastic spheres: the effect of delayed recovery. arXiv:07081434 (2007)
45. Stevens, A.B., Hrenya, C.M.: Comparison of soft-sphere models to measurements of collision properties during normal impacts. Powder Technol. **154**, 99–109 (2005)
46. White, J.A., Borja, R., Fredrich, J.T.: Calculating the effective permeability of sandstone with multiscale lattice Boltzmann/finite element simulations. Acta Geotech. **1**, 195–209 (2006)
47. Wu, C., Li, L., Thornton, C.: Rebound behaviour of spheres for plastic impacts. Int. J. Impact Eng. **28**, 929–946 (2003)
48. Zhang, J., Hu, Z., Ge, W., Zhang, Y., Li, T., Li, J.: Application of the discrete approach to the simulation of size segregation in granular chute flow. Ind. Eng. Chem. Res. **43**, 5521–5528 (2004)
49. Zhou, Y.C., Wright, B.D., Yang, R.Y., Xu, B.H., Yu, A.B.: Rolling friction in the dynamic simulation of sandpile formation. Phys. A **269**, 536–553 (1999)
50. Zhou, Y.C., Xu, B.H., Yu, A.B., Zulli, P.: An experimental and numerical study of the angle of repose of coarse spheres. Powder Technol. **125**, 45–54 (2002)